The phases of the Moon: modelling crystallisation of the lunar magma ocean through equilibrium thermodynamics

T.E. Johnson[a*], L.J. Morrissey[b], A.A. Nemchin[a], N.J. Gardiner[c], J.F. Snape[d]

[a]*School of Earth and Planetary Sciences, The Institute of Geoscience Research, Space Science and Technology Centre, Curtin University, Perth, Western Australia 6102, Australia*

[b]*Future Industries Institute, University of South Australia, Mawson Lakes, South Australia 5095, Australia*

[c]*School of Earth and Environmental Sciences, University of St. Andrews, St. Andrews KT16 9AL, United Kingdom*

[d]*Faculty of Earth and Life Sciences, VU Amsterdam, De Boelelaan 1085, 1081 HV Amsterdam, the Netherlands*

* Corresponding author at: School of Earth and Planetary Sciences, The Institute for Geoscience Research (TIGeR), SSTC, Curtin University, GPO Box U1987, Perth WA 6845, Australia.

E-mail address: tim.johnson@curtin.edu.au (T.E. Johnson).

Keywords: Moon, lunar basalts, lunar magma ocean, lunar mantle, phase equilibrium modelling.

ABSTRACT

Despite some 50 years of intense research on samples returned from the Apollo missions and lunar meteorites, along with remote-sensing and Earth-based observations, many questions regarding the formation and evolution of the Moon persist. These include the detailed compositional and density structure of the lunar mantle and the source and petrogenesis of the diverse suite of extrusive and intrusive igneous rocks. There is broad agreement that the

primary internal structure of the Moon reflects crystallisation of a lunar magma ocean (LMO), and that an inverted density gradient within the mantle cumulates led to some reorganisation of layers by partial convective overturn. Experimental studies have provided invaluable constraints on crystallisation of the LMO, but are limited by the relatively small number of experiments that can practically be undertaken. Here we use recently-developed thermodynamic models for minerals and melt in the K_2O–Na_2O–CaO–FeO–MgO–Al_2O_3–SiO_2–TiO_2–Cr_2O_3 system to model crystallisation of a full-moon LMO based on two existing end-member bulk compositions—Taylor Whole-Moon (TWM), and Lunar Primitive Upper Mantle, LPUM—on which many experimental studies have been based. We follow several recent studies in considering equilibrium crystallisation of the first 50 vol.% and fractional crystallisation thereafter. Our results match well with experimental studies, and provide detailed constraints on the major oxide composition, mineralogy and density structure based on the two starting compositions that, while exhibiting some similarities, show important differences. The more fertile TWM composition contains significant quantities of garnet in the deep mantle, whereas the LPUM composition has none. By contrast, prior to any gravitational overturn, the uppermost mantle cumulates for TWM are strongly silica-undersaturated and contain abundant aluminous spinel, whereas those for LPUM are silica-saturated. For both starting compositions, with the exception of TiO_2 and Na_2O, our modelled compositions of the final dregs of fractionated melt show a reasonable match with existing estimates on the composition of urKREEP. Modelled partial melts of the upper-mantle cumulates at low to moderate melt fractions have major oxide compositions that match well with low- and intermediate-Ti lunar basalts. The correspondence is particularly good for picritic (green) glasses that likely represent melts derived from deeper levels within the upper mantle. The wide spread in TiO_2 concentrations in lunar basalts and basaltic glasses is consistent with density-driven reorganisation involving ilmenite. Our simulations provide

thermodynamically-robust estimates of the compositional, mineralogical and density structure of the lunar interior that are unprecedented in their detail, and which provide the foundation for several lines of future research addressing the origin and secular evolution of the Moon.

1. Introduction

The Moon probably formed through an oblique impact between the Earth and a Mars-sized object (Canup, 2014; Hartmann and Davis, 1975), although the precise timing of the impact is debated (Barboni et al., 2017; Connelly and Bizzarro, 2016; Thiemens et al., 2019). Following the impact, rapid accretion of the ejecta to form the Moon would have led to widescale melting and formation of a lunar magma ocean (LMO) that was at least a few-hundred km thick, but could have been the entire mantle (Elkins-Tanton et al., 2011; Longhi, 2006; Shearer et al., 2006; Warren, 1985). Crystallisation of the LMO over the next tens or hundreds of millions of years (Elkins-Tanton et al., 2011; Nemchin et al., 2009) led to differentiation of the silicate portion into a dense ultramafic to mafic cumulate pile (the lunar mantle) and, after ~70–80 percent solidification (hereafter PCS following Snyder et al., 1992), crystallisation of plagioclase to form an anorthosite flotation crust that ultimately reached a thickness of up to ~60 km (Charlier et al., 2018; Elardo et al., 2011; Elkins-Tanton et al., 2011; Rapp and Draper, 2018; Shearer et al., 2006; Wieczorek et al., 2013). At a late stage (>90 PCS), crystallisation of ilmenite formed Ti-rich cumulates and a residual melt enriched in highly incompatible elements, including the heat-producing elements K, Th and U. This evolved melt likely represents the source of the geochemical signature identified in various lunar lithologies (e.g. KREEP basalts), so-called due to an enrichment in K, the rare

earth elements (REE) and P (Borg et al., 2004; Lin et al., 2017b; Snyder et al., 1992; Warren and Wasson, 1979).

In addition to the pale-coloured anorthosite crust, the surface of the Moon is characterised by numerous dark basalt-filled impact craters (maria) that cover some 15% of the lunar surface, but which comprise <1 vol.% of the crust (Wieczorek et al., 2006). These mare basalts, volcanic glass fragments and older (pre-mare) volcanic and plutonic rocks (Delano, 1986; Snape et al., 2019), are the primary source of information regarding the composition of the mantle cumulates, from which most were derived (Neal and Taylor, 1992; Shearer et al., 2006; Shearer and Papike, 1999). However, whether and what proportion of the basalts formed by direct impact melting, adiabatic melting following density inversion of the cumulate pile, fractional crystallisation or other mechanisms are matters of debate (Faure et al., 1992; Longhi, 1992; Neal et al., 2015; Neal and Taylor, 1992; Shearer and Papike, 1999; Walker et al., 1975). The basalts have traditionally been subdivided based on an apparently bimodal distribution of Ti contents (Neal and Taylor, 1992), suggesting that the lunar mantle is compositionally heterogeneous with respect to Ti (and other elements), likely reflecting a variable abundance of cumulate ilmenite (Giguere et al., 2000; Walker et al., 1975).

Resolving these and other complex questions, including: the origin and role of the KREEP component; the petrogenesis of magnesian lithologies of the Mg-suite and rare rocks containing aluminous spinel; what the compositional variability in lunar basalts tells us about how and from where they were produced, and; whether any lunar rocks are samples of the mantle; requires an understanding of the internal structure of the Moon. However, in detail, the structure, whole-rock and mineralogical composition of the upper mantle from where, as on Earth, most of the basalts were likely derived, is poorly understood.

Our current knowledge of the internal structure of the Moon is largely founded on experimental studies that have investigated crystallisation of the LMO based on a range of

assumptions and starting materials (Charlier et al., 2018; Elardo et al., 2011; Elkins-Tanton et al., 2011; Lin et al., 2020; Lin et al., 2017b; Rapp and Draper, 2018). However, experiments are time-consuming and expensive, each of which represent a single datum in pressure–temperature–composition (*P–T–X*) space. Equilibrium thermodynamics offers a means of extrapolating experimental results seamlessly across *P–T–X* space. Doing so requires (experimentally-constrained) thermodynamic data for the pure end-members and activity–composition (*a–X*) models describing the energetics of mixing in the relevant solid solution minerals.

Here, using the software THERMOCALC (Powell and Holland, 1988), we simulate crystallisation and fractionation of the LMO. The modelling employs the internally-consistent end-member thermodynamic dataset of Holland and Powell (2011) and recently-developed *a–X* models for minerals and melt originally calibrated to investigate partial melting of terrestrial peridotite (Jennings and Holland, 2015) and later extended to permit modelling in larger chemical systems and over a much broader compositional range (Holland et al., 2018). Our approach represents the state-of-the-art with respect to calculated phase equilibria, and permits fully-quantitative modelling of melt-bearing equilibria at all depths within the Moon and other rocky bodies with radii up to ~2000 km.

Our simulations provide a detailed thermodynamically-consistent model of the silicate Moon from the crust to the base of the mantle prior to any gravity-driven reorganisation of the mantle cumulates. The results include the abundance, composition and density of minerals and melt, and the thickness, bulk composition and density within and between the layers that comprise the lunar mantle and crust. The model, which we compare with existing data, provides a direct framework for investigating the major oxide, trace element and isotopic evolution of the crystallised LMO. We demonstrate application of this framework to

the generation of mantle-derived melts produced by partial melting of the cumulates, with implications for the origin of lunar basalts and the wider secular evolution of the Moon.

2. Methods

In modelling the crystallisation of a lunar magma ocean (LMO), we follow an approach similar to that used in several previous studies (Elardo et al., 2011; Snyder et al., 1992; Spera, 1992; Tonks and Melosh, 1990). We assume a silicate LMO that is initially entirely molten and which cools and crystallises thereafter in two fundamentally different steps, first through equilibrium crystallisation then by fractional crystallization (Fig. 1). Following Elardo et al. (2011), we model two bulk compositions that are near-identical to the Taylor Whole Moon (TWM; Taylor (1982)) and Lunar Primitive Upper Mantle (LPUM; Longhi (2006)) bulk silicate Moon compositions, which represent relatively enriched and depleted end members, respectively. However, to enable a direct comparison, our modelled compositions are identical (with respect to the major element oxides) to the corresponding TWM and LPUM starting powders used in the equilibrium crystallisation experiments of Elardo et al. (2011) (their table 1) and, for LPUM, the fractional crystallisation experiments of Rapp and Draper (2018). The TWM composition used here has 2.4 wt% less FeO than the original composition of Taylor (1982) to account for the likely presence of a small core (0.7–0.9% by volume (Weber et al., 2011).

All calculations were performed via THERMOCALC 3.50 (Powell and Holland, 1988). Although the *a–X* models of Holland et al. (2018) permit calculations in the K_2O–Na_2O–CaO–FeO–MgO–Al_2O_3–SiO_2–H_2O–TiO_2–Fe_2O_3–Cr_2O_3 (KNCFMASHTOCr) chemical system, we use an anhydrous and ferric iron-free subset (i.e., in the KNCFMASTCr system),

consistent with oxygen fugacities below the iron–wüstite buffer (Wieczorek et al., 2006) and the absence of hydrous minerals, with the possible exception of apatite (McCubbin et al., 2010). We consider the phases olivine, orthopyroxene, pigeonite (low-Ca clinopyroxene), augite (high-Ca clinopyroxene), spinel *sensu lato*, plagioclase, quartz, ilmenite and melt. The *a–X* model for olivine currently does not include Cr, such that our simulations may overestimate the stability and abundance of Cr-rich spinel (magnesiochromite or chromite), although this is only ever present in very low abundances (< or <<1 vol.%). Phase abbreviations follow Whitney and Evans (2010).

Throughout, we assume that the convective geotherm (adiabat) lies between, and is roughly parallel to, the solidus and liquidus throughout the crystallisation interval and at all depths within the LMO such that the overall volume of crystals and melt is identical at all depths. Although undoubtedly a simplification, this is a reasonable first-order assumption (Elardo et al., 2011; Tonks and Melosh, 1990). Justification for the two-stage crystallization model and other assumptions are provided in the Electronic Annex of Elardo et al. (2011) and references therein. Additional details of our model approach are summarised below (see also Fig. 1 and Supplementary Tables 1 and 2).

During the initial stage of equilibrium crystallization (Stage 0), crystals remain suspended within a vigorously convecting magma until the solid (crystal) fraction reaches 50 vol.%. At that point we calculate the abundance, composition and density of minerals, and the composition and density of the melt, at twenty equally-spaced pressure intervals (depths) throughout the whole silicate LMO (i.e., from 0.001–4.5 GPa), then 'sink' the (olivine-dominated) crystal fraction to form a thick cumulate pile whose upper surface lies at a pressure of 1.73 GPa, corresponding to a depth of ~360 km assuming an average density of 3.35 g cm^{-3} (Wieczorek et al., 2006). Here and in subsequent steps, we assume that all crystals settle at an identical velocity such that those that formed at the base of the LMO

settle first to form the bottommost layer of the cumulate pile, and vice versa. We then simulate fractional crystallization of the remaining 50 vol.% melt in ten stages (stages 1–10), in each case crystallising an identical volume of melt (i.e. 5 vol.% of the starting volume of the LMO). During each stage, we calculate the abundance, composition and density of minerals, and the composition and density of melt, at ten equally-spaced pressures (depths) within the remaining magma at the appropriate melt fraction (Fig. 1). With the exception of plagioclase and quartz, all other minerals are considered to sink to the base of the magma, adding to the thickness of the cumulate pile. If plagioclase and/or quartz form, they are moved to the top of the remaining LMO to form a 'flotation' crust. The next stage considers fractional crystallization of the remaining layer of melt that is bound at its base by the top of the cumulate pile and at its top by the surface or the base of the 'flotation' crust, and so on until no melt remains.

Each stage of the calculations uses a new starting melt composition, which is taken to be the average composition of melt over the ten equally-spaced pressure increments modelled during the preceding stage (see Supplementary Tables 1 and 2). To constrain the compositional and density structure of the upper mantle, and the potential source compositions for lunar basalts and glasses, we also calculate the composition of the solid residue that forms the cumulate pile for that stage, based on the calculated abundance and composition of the minerals (excluding plagioclase), weighted across the ten substages. Importantly, we also include in the residue 3 vol.% trapped (intercumulus) melt and 3% of any plagioclase that formed during that stage, values that are similar to those (1–5% melt and 2–5% plagioclase) considered by Snyder et al. (1992).

3. Results

Detailed results including the starting bulk compositions (as mol.% oxide), proportions, compositions (as mol.% oxide) and densities (as $g.cm^{-3}$) of minerals, melts and residues calculated during each stage of the model as a function of temperature (*T*) and pressure (*P*) are provided in Supplementary Tables 1 and 2.

3.1. Equilibrium crystallisation (Stage 0)

Phase equilibria for the two modelled silicate LMO starting bulk compositions TWM and LPUM are shown in Fig. 2a and b, respectively. Although these diagrams are broadly similar, they exhibit some important differences. For both compositions, olivine is the first mineral to crystallise on cooling of the LMO except at $P > 4$ GPa for TWM, where orthopyroxene appears first. Compared to LPUM, liquidus temperatures for TWM are lower by between 50 ºC (1920 vs 1870 ºC at 4.5 GPa) and 80 ºC (1800 vs 1720 ºC at 0.01 GPa). For the TWM composition, at $P < 3.3$ GPa, a spinel group mineral (here magnesiochromite) begins to crystallise next, followed by orthopyroxene. On cooling further, the next mineral to appear is garnet at $P > 1.8$ GPa, clinopyroxene between ~1.8 and 0.7 GPa, and plagioclase at $P < 0.7$ GPa (Fig. 2a). For LPUM, orthopyroxene joins olivine as the next mineral to crystallise across the entire modelled pressure range, followed by garnet at $P > 2.7$ GPa, clinopyroxene between 2.7 and 0.5 GPa, and plagioclase at lower pressures. The temperature of final crystallisation (solidus) for the two compositions is similar, and high *T* subsolidus assemblages comprise Ol–Opx–Cpx with plagioclase at low *P* (<0.7–0.8 GPa), garnet at high *P* (>1.5–2.0 GPa) and spinel (magnesiochromite/chromite) at intermediate *P* (Fig. 2). The subsolidus fields of coexisting plagioclase and spinel at lower *P*, and spinel and garnet at higher *P*, extend over a significantly wider pressure range in TWM relative to LPUM.

The composition, abundance and density of minerals and melt at Stage 0 of the model are controlled by phase equilibria along the 50 mol.% melt isopleth, shown by the bold dashed white line on Fig. 2a and b (mol.% values output by THERMOCALC approximate vol.%). This isopleth occurs at significantly lower *T* for TWM than for LPUM, by between ~90 ºC at 4.5 GPa (~1730 vs 1820 ºC, respectively) and 160 ºC at 0.01 GPa (~1450 ºC versus 1610 ºC, respectively), reflecting the more fertile nature of the TWM composition. An important first-order consequence is that garnet is predicted to be stable at high *P* (>3.4 GPa) in TWM during Stage 0 (Snyder et al., 1992), but none forms in LPUM (Fig. 2).

As described above, prior to the initial stage of fractional crystallisation (Stage 1), all minerals are settled to the base of the LMO to form a cumulate pile, which extends from the core–mantle boundary at 4.50 GPa (~1400 km depth) to 1.73 GPa (~360 km depth). The calculated abundance (coloured fields as mol.% ~vol.%, black scale at the base), composition (*X*; solid coloured lines as mole/atomic fraction, orange scale at the top; for olivine, orthopyroxene, garnet and melt, $X = X_{Mg}$ = atomic Mg/(Mg + Fe); for spinel, $X = X_{Chr}$ = atomic Cr/(Cr + Al)) and density (ρ; dashed coloured lines in $g.cm^{-3}$, blue scale at the top) of the Stage 0 cumulate for the two bulk compositions are shown in Fig. 3, along with the composition and density of melt. For TWM (Fig. 3a), the cumulate pile contains ~17 mol.% garnet and ~30 mol.% orthopyroxene at its base. The amount of garnet decreases with decreasing pressure (depth) until it disappears at ~3.8 GPa. The abundance of orthopyroxene decreases with decreasing *P* until it disappears at ~2.2 GPa. A small quantity of magnesiochromite (<1 mol.%) occurs at pressures of 3.7 GPa and less. For LPUM (Fig. 3b), the cumulate comprises 45 mol.% orthopyroxene and 55 mol.% olivine at its base, with the abundance of orthopyroxene decreasing with decreasing pressure until the cumulate becomes pure dunite at $P < 2.5$ GPa.

In terms of mineral chemistry, olivine and orthopyroxene compositions in TWM are essentially constant from the base to the top of the cumulate (X_{Ol} = 0.91 to 0.90; X_{Opx} = 0.93 to 0.91), whereas melt becomes less magnesian (X_{Liq} = 0.77 to 0.71). At the base of the cumulate, garnet compositions are constant (X_{Grt} = 0.88), and spinel compositions become significantly enriched in the chromite component (X_{Spl} = 0.56–0.80) and enriched in Fe^{2+} (X_{Mg} = 0.73–0.65) with decreasing pressure. For LPUM, olivine and orthopyroxene are slightly more magnesian than in TWM (X_{Ol} = 0.94–0.95; X_{Opx} = 0.95). For both compositions, all minerals are denser than coexisting melt, although at the base of the cumulate pile the difference is small (Fig. 3).

3.2. Fractional crystallisation (Stages 1–10)

The calculated abundances of minerals in equilibrium with melt at each stage of fractional crystallisation of the remaining 50 vol.% of the LMO for the two compositions are summarised in Fig. 4, along with cumulate stratigraphies proposed by others, although none of these existing studies provides a direct comparison with our calculations. During Stage 1 (50–55 PCS), the remaining LMO extends from pressures of 1.73 GPa (P_{max}) to the surface (P_{min}). For TWM, the crystal fraction is mostly olivine with a small amount of orthopyroxene near the base. For LPUM, only olivine grows during Stage 1. In both cases, the solid fraction sinks, reducing P_{max} in Stage 2 to 1.54 GPa, and a new melt composition is calculated. During stages 2 and 3 (55–65 PCS), a small quantity of magnesiochromite forms in both compositions, and the proportion of orthopyroxene increases and olivine decreases, with relatively more orthopyroxene in TWM.

At Stage 4 (65–70 PCS), the evolutions of the two compositions diverge. For stages 4 and 5 for LPUM, the cumulate is harzburgite with minor magnesiochromite, in which the

proportion of orthopyroxene continues to increase. However, for TWM, Stage 3 marks the end of orthopyroxene crystallisation, and Stage 4 records growth of significant quantities of pigeonite that coexists with olivine and magnesiochromite. Stage 5 (70–75 PCS) for the TWM composition marks the first appearance of plagioclase and high-Ca clinopyroxene (hereafter clinopyroxene), which coexist with pigeonite but no olivine. Although the pyroxenes sink, further decreasing P_{max} during Stage 6 (to 0.89 GPa), the plagioclase is floated to the top of the remaining LMO, increasing P_{min} (to 0.08 GPa) during Stage 6. For TWM, stages 5 to 8 (70–90 PCS) are characterised by a solid assemblage of Pig–Cpx–Pl, in which the proportion of clinopyroxene increases relative to pigeonite and plagioclase. A small quantity of ilmenite first appears during Stage 8 (85–90 PCS), with its abundance increasing during Stage 9, where ilmenite coexists with plagioclase and clinopyroxene but no pigeonite. For LPUM, plagioclase first crystallises with orthopyroxene and olivine during Stage 6 (75–80 PCS). Pigeonite and clinopyroxene first appear at Stage 7, in which the solid fraction is ~50 mol.% plagioclase and the proportion of orthopyroxene is greatly reduced. For LPUM, stages 8 and 9 (85–95 PCS) comprise subequal quantities of pigeonite, clinopyroxene and plagioclase, with ilmenite first growing during Stage 9.

Crystallisation of the final remaining 5% of the original LMO (Stage 10) for the two starting bulk compositions forms a layer with very different bulk compositions and mineral assemblages. For TWM, the bulk composition of Stage 10 is silica-undersaturated and comprises ~50 mol.% clinopyroxene with Fe-rich olivine, Fe–Al-rich spinel (hercynite) and minor plagioclase. For LPUM, the Stage 10 bulk composition is silica-saturated and on crystallisation contains subequal quantities of pigeonite, clinopyroxene, plagioclase and quartz.

3.3. Post-LMO solidification

The sequence and mineralogy of the cumulate layers produced by fractional crystallisation of the two bulk compositions (i.e. stages 1–10), which together comprise the upper mantle and flotation crust, is shown in Fig. 5a. The pressure at the base of each layer is the P_{max} for that layer as shown in Fig. 4, whereas the pressure at its top is the P_{max} for the overlying layer. The pressure at the lunar Moho, and thereby the thickness of the anorthosite flotation crust, is not significantly different for TWM and LPUM (0.29 GPa and 0.26 GPa, respectively; Fig. 5a). However, whereas the TWM crust is here taken to be a monomineralic layer of plagioclase, the LPUM crust contains minor (<1 vol.%) quartz.

The composition (X) and density (ρ) of minerals and melt within the upper mantle cumulates are shown in Fig. 5b and c, respectively, for which $X_{Pl} = X_{An}$ = atomic Ca/(Ca + Na + K). The higher X_{Mg} of the LPUM composition means that, at any particular stage, the X_{Mg} of the minerals is higher than in TWM (Fig. 5b). For ferromagnesian silicates in equilibrium, $X_{Opx} \geq X_{Ol} > X_{Cpx} \geq X_{Pig} > X_{Liq}$, except for the Stage 10 cumulate for TWM, where fayalitic olivine (X_{Mg} = 0.21) is less magnesian than coexisting clinopyroxene (X_{Mg} = 0.34–0.33). The solid solution minerals become more ferroan (for olivine, the pyroxenes, spinel and melt), more aluminous (for spinel) and more sodic (for plagioclase) as fractional crystallisation proceeds (Fig. 5b). Throughout stages 6 to 10 for LPUM, plagioclase is anorthite, with X_{Pl} ranging from 0.99 (Stage 6) to 0.94 (Stage 10). For the TWM starting composition, plagioclase is anorthite from stage 5 to 9 (X_{Pl} = 0.99 to 0.97), but andesine (X_{Pl} = 0.34) during Stage 10 (Fig. 5b). During the early stages of fractionation of both compositions, the first spinel to grow is magnesiochromite ($X_{Mg} > 0.5$) that incorporates increasing quantities of Al and Fe. In Stage 4 for TWM, the uppermost spinel is chromite (X_{Mg} = 0.47) but magnesiochromite at lower levels. Spinel grown during TWM Stage 10 is Cr-free hercynite (X_{Mg} = 0.14–0.15).

The decrease in X_{Mg} of the ferromagnesian minerals with increasing degree of fractionation leads to a concomitant increase in their density (Fig. 5c). Although generally present in small quantities, the densities of spinel (~4.0 g cm^{-3}) and ilmenite (4.6 g cm^{-3}) are significantly higher than the other minerals. In decreasing order, the density of the minerals is Ilm > Spl > Ol ≥ Opx ≥ Pig ≥ Cpx > Liq > Pl, except during crystallisation of the final dregs of melt for the LPUM starting composition where plagioclase is marginally denser than coexisting melt (Fig. 5c).

3.4. Compositional evolution of melt and residues

The calculated average major oxide bulk composition (in wt%), and X_{Mg} (in mole fraction) of the melt (in red) and cumulate residue (in blue, which include 3% intercumulus melt and 3% of any plagioclase that grows) formed during stages 0–10 for the TWM (left) and LPUM (right) starting compositions, and plotted against MgO content, are shown in Fig. 6, along with a quadratic line of best fit between data points. The initial bulk compositions of TWM and LPUM are shown as grey squares that (as mass balance demands) are colinear with, and equidistant from, the Stage 0 melts and residues (Fig. 6).

The calculated evolutions of the two compositions show broad similarities but important differences that become most pronounced during the latter stages of fractionation. Melt compositions from Stage 0 to Stage 10 decrease in MgO content and X_{Mg}. During the first five (0 to 4 for TWM) and seven (0–6 for LPUM) stages, melt compositions become progressively enriched in all other oxides as fractionation proceeds (Fig. 6). As plagioclase and pyroxenes crystallise, for most oxides, these compositional trends show a sharp inflection, leading to a decrease in SiO_2, TiO_2, Al_2O_3, and CaO, and an increase in FeO, K_2O and Na_2O in melt compositions. For some oxides, a second inflection occurs towards the end

of the fractionation sequence due to the growth of ilmenite (that depletes melt in TiO_2 and FeO). The calculated compositions of the final melts to crystallise are very different. Compared to equivalent melts formed from the TWM composition, Stage 10 melts for LPUM are significantly enriched in SiO_2 (72.6 vs 52.1 wt%), TiO_2 (0.24 vs 0.05 wt%) and FeO (12.1 vs 7.2 wt%), but depleted in Al_2O_3 (6.0 vs 21.3 wt%), K_2O (1.1 vs 3.2 wt%) and Na_2O (1.0 vs 8.5 wt%).

For both compositions, the calculated bulk compositions of Stage 1 residues are marginally enriched in MgO relative to Stage 0 cumulates (Fig. 6). During fractional crystallisation thereafter (stages 1–10), the residues become successively depleted in MgO and record decreasing X_{Mg}. Although the Stage 10 residues differ significantly, for most oxides the compositional evolution of the two starting compositions follows similar patterns (in terms of increasing or decreasing abundance and inflection points) that, with the exception of Al_2O_3 and TiO_2, broadly mimics those of melt compositions. Relative to residue compositions during the early stages of fractionation, late-stage residues are significantly enriched in CaO, FeO, K_2O and Na_2O. Notably, Stage 10 residues for the TWM starting composition show extreme enrichment in K_2O (3.2 wt%) and Na_2O (8.5 wt%). Concentrations of TiO_2 in TWM increase until Stage 8, but decrease thereafter to 0.3 wt% in Stage 10. By contrast, in LPUM, TiO_2 contents mostly increase with increasing degrees of fractionation, reaching extreme values (4.6 wt%) during Stage 10. Stage 10 residues for TWM are significantly enriched in Al_2O_3 relative to LPUM (13.8 vs 2.9 wt%), but depleted in SiO_2 (37.2 vs 46.2 wt%).

4. Discussion

4.1. Comparison with experiments

Our calculations for equilibrium crystallisation of the first 50 vol.% of a full-moon LMO from both the TWM and LPUM starting compositions match well with the experimental results of Elardo et al. (2011) (compare Fig. 4 with fig. 3 of (Rapp and Draper, 2018). However, for TWM our models (Fig. 2) indicate that orthopyroxene, not olivine, is the first mineral to crystallise at extreme depths (>4 GPa). The small amounts of magnesiochromite predicted at higher pressures may be an artefact reflecting the lack of Cr in the *a–X* model for olivine. As in the experiments of Elardo et al. (2011), garnet is stable at the base of the cumulate pile, consistent with the trace element compositions of some lunar glass beads (Neal, 2001). The presence of harzburgite in the base of the Stage 0 cumulates is consistent with the experiments of Lin et al. (2017b), although their starting compositions contained no Na_2O, K_2O or Cr_2O_3. For both starting compositions, our calculated compositions of olivine, orthopyroxene and garnet are a good match with those of Elardo et al. (2011) (compare their Appendix A with our Stage 0 calculations in Supplementary Tables 1 and 2).

Our stepwise calculations simulating fractional crystallisation of the upper 50 vol.% of the LMO are not directly comparable with the experimental results summarised in fig. 3 of Rapp and Draper (2018), in which the entire LMO was considered to have evolved via fractional crystallisation. Consequently, for both TWM and LPUM, the experiments indicate a lower cumulate pile (corresponding to our Stage 0) consisting of pure olivine, but less olivine, orthopyroxene and pigeonite in the upper 50 vol.% than stage 1–10 of our models (Fig. 4). Although Charlier et al. (2018) assumed a lower mantle (below 600 km) comprising pure olivine for all three of their starting compositions (LPUM, TWM and the composition of O'Neill, 1991), our calculated upper mantle cumulate stratigraphy is a reasonable match with theirs (Fig. 4).

4.2. Density structure

The calculated average bulk density of the layers produced during stages 0–10 is shown in Fig. 7. As shown in previous studies (Elkins-Tanton et al., 2011; Hess and Parmentier, 1995; Shearer et al., 2006; Shearer and Papike, 1999; Solomatov, 2000), the density of the cumulate increases as fractionation proceeds, predominantly due to a decrease in temperature, an increase in Fe content (decrease in X_{Mg}) of the main silicate minerals, the late crystallisation of ilmenite (beginning at ~85–90 PCS) and, in the case of TWM, Fe–Al-rich spinel. Our modelling suggests formation of small quantities of magnesiochromite earlier than in most other models, which likely reflect the absence of Cr from the *a–X* model for olivine (Figs 3 and 4).

The gravitational instability implied by the density profile shown in Fig. 7 is a reasonable match with that of Elkins-Tanton et al. (2011) makes overturn of the cumulate pile driven by Raleigh–Taylor instabilities possible, or even likely (Elkins-Tanton et al., 2011; Hess and Parmentier, 1995; Solomatov, 2000; Wieczorek et al., 2006). However, the physics involved is a complex function of temperature, mineral compositions and densities, melt fraction and non-linear stress-dependent rheologies that make predicting the structure of any post-overturn lunar mantle somewhat speculative (Elkins-Tanton et al., 2011; Wieczorek et al., 2006) and beyond the scope of the current study.

4.3. Compositional structure

4.3.1. The anorthosite crust

Our simulations produce an anorthosite crust with a thickness of ~50–55 km for both the TWM and LPUM starting compositions, values that are higher than the average value (34–43 km) proposed based on high-resolution gravity data from the Gravity Recovery and Interior Laboratory (GRAIL) mission (Wieczorek et al., 2013; Zuber et al., 2013). Our calculated crustal thicknesses are lower than early estimates (Taylor, 1982; Toksőz et al., 1972) and those of some experimental studies (Lin et al., 2017b), but similar to estimates based on various chemical and physical constraints (Elkins-Tanton et al., 2011) and those derived from experiments considering fractional crystallisation of the entire LMO (Rapp and Draper, 2018). Compared to the GRAIL data, a greater thickness for the anorthosite crust here and in other studies may reflect the presence of small quantities of H_2O that has been shown experimentally to suppress plagioclase crystallization (Lin et al., 2017a). Alternatively, a thinner anorthosite crust is predicted to form in our models when considering a greater quantity (>3%) of intercumulus melt or plagioclase entrained within the mantle cumulates.

Assuming that the anorthosite flotation crust had its oldest portions nearest the surface and was underplated by subsequent flotation products (Elkins-Tanton et al., 2011), the LPUM anorthite crust shows reverse layering, and to be near pure anorthite (X_{An} = 0.99) at its top becoming more progressively more sodic towards its base (X_{An} = 0.94). The base of the crust for LPUM should also contain quartz, consistent with the experiments of (Charlier et al., 2018). A similar zonation is expected throughout most of the thickness of the anorthosite crust for TWM (X_{An} = 0.99 to 0.97), with the addition of a thin lowermost layer of andesine, but no quartz. The calculated compositions of plagioclase throughout most of the anorthosite crust are similar to those measured in samples of ferroan anorthosite (Warren, 1993; Wieczorek et al., 2006).

4.3.2. The lunar mantle

Immediately underlying the anorthosite crust, prior to any potential gravity overturn, the uppermost cumulate layers (Stage 10) for the TWM and LPUM compositions have distinct mineralogies and bulk compositions (Figs 4–6). An obvious question that arises is whether or not any of the existing mafic/ultramafic plutonic rocks from the Moon represent samples of the lunar mantle. The majority of old (4.5–4.4 Ga) mafic–ultramafic lunar plutonic rocks are Mg-rich rocks that likely represent the products of intracrustal fractional crystallisation of basaltic magmas derived from the upper mantle rather than samples of the mantle per se (Shearer et al., 2015). Rare aluminous spinel-bearing troctolites have been proposed to represent samples of lowermost crust or upper mantle (Gross et al., 2014). Although our modelling of the TWM starting composition has an uppermost cumulate layer (Stage 10) containing abundant aluminous spinel (Fig. 5), these rocks have bulk compositions that are too aluminous, and contain spinel and olivine that are much too magnesian, to be primary mantle cumulates, and their origin is likely more complex (Prissel et al., 2014).

Similarly, there is no clear evidence for the existence of samples that might represent the pyroxenites and dunites predicted by our simulations to form in the upper and lower mantle, respectively (Fig. 5). Although mineral aggregates that superficially resemble such rocks occur as clasts within several lunar breccias, they are strongly recrystallised and/or preserve clear disequilibrium features such that their origin is ambiguous (Beaty and Albee, 1980; Papanastassiou and Wasserburg, 1975). Intriguingly, reaction microstructures within some of these samples have been interpreted to represent replacement of garnet (Beaty and Albee, 1980; Papanastassiou and Wasserburg, 1975), and may lend support for the presence of garnet in the deep mantle (Neal, 2001), consistent with our calculations based on the TWM starting composition (Figs 2, 3).

4.3.3. Fractionated melts and the origin of KREEP

Some KREEP basalts are considered to represent fractionated or contaminated products of the most evolved melts formed during the final stages of fractional crystallisation of the LMO at ~99 PCS (Warren, 1985; Warren and Wasson, 1979). Two compositions proposed for the primary KREEP melt, so-called urKREEP (Neal and Taylor, 1989b), are shown on Fig. 6—these should be equivalent to our Stage 10 modelled melts. For the TWM starting composition, the modelled melts show a reasonable match with the urKREEP compositions in terms of MgO, SiO_2, and K_2O, but a poor match for TiO_2, CaO and FeO (much higher in urKREEP) and Al_2O_3, Na_2O and X_{Mg} (much lower in urKREEP). For the LPUM starting composition, the correspondence is good for Al_2O_3 and K_2O, and much better for FeO, Na_2O and X_{Mg}, but less good for SiO_2. Whether these differences reflect density-driven reorganisation of the upper mantle, infelicities in the thermodynamic models, or something else, is not clear. However, it is worthwhile noting that KREEP-like basalts are highly variable in composition, and likely record varied and complex processes (Korotev et al., 2011).

4.4. Partial melting of the cumulates and lunar basalts – major oxide geochemistry

A potentially powerful application of our approach is in providing constraints on the compositions of primary unfractionated mantle-derived melts produced by subsequent partial melting of cumulates, with implications for the origin of lunar basalts. As a first step, we calculated pressure–temperature phase diagrams for the modelled compositions of the cumulates produced during stages 0–10 for the TWM and LPUM starting compositions assuming no density-driven overturn (i.e. between P_{max} and P_{min} in Fig. 4). The results are summarised in Fig. 8, in which is shown the mineral assemblage and the *P–T* conditions of

the solidus (thick black line) and the liquidus (thick white line) for each cumulate layer. Upon heating, a transition from a darker to a paler field corresponds to the appearance of a new mineral, whereas a transition from a paler to a darker field indicates the loss of a mineral (in each case, the relevant mineral is labelled). For both compositions, the solidus temperature, liquidus temperatures and melting interval decrease with increasing degree of fractionation from Stage 1 to Stage 10. In the suprasolidus fields, pigeonite, clinopyroxene and plagioclase are stable at a lower degree of fractionation in TWM relative to LPUM, consistent with its more fertile composition.

From these phase diagrams, we calculated the major oxide composition of the (mostly basaltic) melts formed within each cumulate layer on heating to produce melt fractions (F) of 0.05, 0.1, 0.2 and 0.3 (white dots on Fig. 8; see Supplementary Table 3), with the pressure of melting taken to be the mid-point of that layer. At any particular degree of fractionation (Stage), these melt fractions are produced at significantly lower temperature in the more fertile TWM starting composition relative to LPUM. For example, Stage 10 melts in TWM between ~900 ºC (F = 0.05) and 1000 ºC (F = 0.30), whereas Stage 10 melts of LPUM cumulates require T > 1100 ºC (Fig. 8).

The calculated composition of the melts are shown in Fig. 9, along with smoothed kernel density estimates of the compositions of lunar basalts taken from the ApolloBasalt DB(v2) database (https://people.mines.edu/kcone/apollobasaltdb_v2_2020/), which were filtered to exclude regolith samples and those with major oxide totals <98 wt%. Although more complex classification schemes for lunar basalts have been devised (Neal and Taylor, 1992), we here use a simple subdivision into low-Ti (including very low-Ti; n = 446; blue clouds on Fig. 6), intermediate-Ti (n = 10; green clouds), high-Ti (including very high-Ti; n = 163; pink clouds) and KREEP-like (n = 70; orange clouds). In addition, we show a smoothed kernel density estimate for the composition of 25 pristine picritic (‘green’) glasses (Delano,

1986) that are the most primitive lunar melts known and which argued to represent the best candidates for primary (unfractionated) melts of deep (~2 GPa) mantle cumulates with variable degrees of assimilation of shallower mantle cumulates (Elkins-Tanton et al., 2003).

Accepting the limitations of the model, it is clear that, most lunar basalts, like terrestrial basalts, do not represent primary mantle melts but products of fractional crystallisation, with or without assimilation of mantle and crustal lithologies (Neal and Taylor, 1992). For most major oxides, melt compositions at moderate to high degrees of fractionation (mostly stages 5–10) are a good match for the measured compositions of low- and intermediate-Ti lunar basalts (blue and green clouds in Fig. 8). Although none of the lunar basalts have compositions suggesting they were derived from the olivine- and orthopyroxene-rich cumulates predicted to form during the earlier stages of crystallisation of the LMO, some of the picritic ('green') glasses (lime green clouds) do. In particular, for most oxides, those with highest MgO and SiO_2, but lowest TiO_2, FeO and Cr_2O_3 contents are a good match for melts of the intermediate (stages 3–6) upper mantle cumulates.

The concentrations of TiO_2 in the modelled melts are significantly lower than in the majority of lunar basalts and the green glasses with lower MgO and SiO_2 contents, which may have TiO_2 concentrations as high as 16.4 wt% (Delano, 1986). These high-Ti glasses, as well as the high-Ti basalts, indicate an important role for fractionation of ilmenite, which is (with spinel) by far the densest mineral present. Overall, these data are consistent with compositional modification of the cumulates by Raleigh–Taylor instabilities driven by density contrasts between layers (Elkins-Tanton et al., 2011; Hess and Parmentier, 1995). Providing more detailed quantitative constraints on these and other processes awaits numerical modelling these density contrasts, and extension of our models to include fractionation of the primary melts and trace element and isotopic modelling.

5. Conclusions

The generally good correspondence between the order of growth, abundance and composition of minerals modelled here with those produced in equivalent experimental studies indicates that the thermodynamic models of Holland et al. (2018) provide a powerful means of quantitatively investigating crystallisation/melting of the silicate portion of rocky bodies with radii of ~2000 km or less. Our results provide detailed estimates regarding the compositional and density structure of the lunar mantle and crust, and on the composition of primary mantle-derived melts, which provide the foundation for future research.

Our approach can be extended to estimate the trace element composition of the primary mantle-derived basaltic melts, and to model their subsequent fractionation, the results of which can be compared to the extensive database of major and trace element bulk-rock compositions of lunar basalts to test existing petrogenetic models. In addition, with appropriate estimates of rheology, the calculated density of minerals and melt can be used in 2D and 3D numerical simulations to constrain the likelihood and extent of mantle overturn during and immediately following crystallisation of the LMO. Our simulations also permit the secular evolution of various radiogenic isotopic systems to be calculated. Finally, our predictions regarding the evolved compositions of the upper mantle cumulates can be used to guide future experimental strategies without the need to simulate the full range of LMO crystallisation.

6. Acknowledgements

TEJ acknowledges support from the State Key Laboratory for Geological Processes and Mineral Resources, China University of Geosciences, Wuhan (Open Fund GPMR201903). We thank J. B. Balta and T. Prissel for their challenging reviews that led to significant improvements in the final version.

7. References

Barboni, M., Boehnke, P., Keller, B., Kohl, I.E., Schoene, B., Young, E.D., McKeegan, K.D., 2017. Early formation of the Moon 4.51 billion years ago. Science Advances 3.

Beaty, D., Albee, A., 1980. The petrology of a pyroxenite xenolith in mare basalt 10050, Lunar and Planetary Science Conference, pp. 67-69.

Borg, L.E., Shearer, C.K., Asmerom, Y., Papike, J.J., 2004. Prolonged KREEP magmatism on the Moon indicated by the youngest dated lunar igneous rock. Nature 432, 209-211.

Buck, W.R., Toksoz, M., 1980. The bulk composition of the Moon based on geophysical constraints, Lunar and Planetary Science Conference Proceedings, pp. 2043-2058.

Canup, R.M., 2014. Lunar-forming impacts: Processes and alternatives. Philosophical Transactions of the Royal Society A: Mathematical, Physical and Engineering Sciences 372.

Charlier, B., Grove, T.L., Namur, O., Holtz, F., 2018. Crystallization of the lunar magma ocean and the primordial mantle-crust differentiation of the Moon. Geochimica et Cosmochimica Acta 234, 50-69.

Connelly, J., Bizzarro, M., 2016. Lead isotope evidence for a young formation age of the Earth–Moon system. Earth and Planetary Science Letters 452, 36-43.

Delano, J.W., 1986. Pristine lunar glasses: Criteria, data, and implications. Journal of Geophysical Research: Solid Earth 91, 201-213.

Elardo, S.M., Draper, D.S., Shearer, C.K., 2011. Lunar Magma Ocean crystallization revisited: Bulk composition, early cumulate mineralogy, and the source regions of the highlands Mg-suite. Geochimica et Cosmochimica Acta 75, 3024-3045.

Elkins-Tanton, L.T., Burgess, S., Yin, Q.Z., 2011. The lunar magma ocean: Reconciling the solidification process with lunar petrology and geochronology. Earth and Planetary Science Letters 304, 326-336.

Elkins-Tanton, L.T., Chatterjee, N., Grove, T.L., 2003. Experimental and petrological constraints on lunar differentiation from the Apollo 15 green picritic glasses. Meteoritics and Planetary Science 38, 515-527.

Faure, G., Hess, P.C., Taylor, S.R., 1992. Mare volcanism and basalt petrogenesis. Geochimica et Cosmochimica Acta 56, 2153-2265.

Giguere, T.A., Taylor, G.J., HAWKE, B.R., Lucey, P.G., 2000. The titanium contents of lunar mare basalts. Meteoritics & Planetary Science 35, 193-200.

Gross, J., Isaacson, P.J., Treiman, A.H., Le, L., Gorman, J.K., 2014. The second conference on the lunar highlands crust and new directions. Spinel-rich lithologies in the lunar highland crust: Linking lunar samples with crystallization experiments and remote sensing. American Mineralogist 99, 1849-1859.

Hartmann, W.K., Davis, D.R., 1975. Satellite-sized planetesimals and lunar origin. Icarus 24, 504-515.

Hess, P.C., Parmentier, E.M., 1995. A model for the thermal and chemical evolution of the Moon's interior: implications for the onset of mare volcanism. Earth and Planetary Science Letters 134, 501-514.

Holland, T., Powell, R., 2011. An improved and extended internally consistent thermodynamic dataset for phases of petrological interest, involving a new equation of state for solids. Journal of Metamorphic Geology 29, 333-383.

Holland, T.J., Green, E.C., Powell, R., 2018. Melting of peridotites through to granites: a simple thermodynamic model in the system KNCFMASHTOCr. Journal of Petrology 59, 881-900.

Jennings, E.S., Holland, T.J., 2015. A simple thermodynamic model for melting of peridotite in the system NCFMASOCr. Journal of Petrology 56, 869-892.

Korotev, R.L., Jolliff, B.L., Zeigler, R.A., Seddio, S.M., Haskin, L.A., 2011. Apollo 12 revisited. Geochimica et Cosmochimica Acta 75, 1540-1573.

Lin, Y., Hui, H., Xia, X., Shang, S., van Westrenen, W., 2020. Experimental constraints on the solidification of a hydrous lunar magma ocean. Meteoritics and Planetary Science 55, 207-230.

Lin, Y., Tronche, E.J., Steenstra, E.S., Van Westrenen, W., 2017a. Evidence for an early wet Moon from experimental crystallization of the lunar magma ocean. Nature Geoscience 10, 14-18.

Lin, Y., Tronche, E.J., Steenstra, E.S., van Westrenen, W., 2017b. Experimental constraints on the solidification of a nominally dry lunar magma ocean. Earth and Planetary Science Letters 471, 104-116.

Longhi, J., 1992. Experimental petrology and petrogenesis of mare volcanics. Geochimica et Cosmochimica Acta 56, 2235-2251.

Longhi, J., 2006. Petrogenesis of picritic mare magmas: Constraints on the extent of early lunar differentiation. Geochimica et Cosmochimica Acta 70, 5919-5934.

McCubbin, F.M., Steele, A., Hauri, E.H., Nekvasil, H., Yamashita, S., Hemley, R.J., 2010. Nominally hydrous magmatism on the Moon. Proceedings of the National Academy of Sciences 107, 11223-11228.

Neal, C., Taylor, L., 1989a. Definition of Pristing, Unadulterated urKREEP Composition Using the" K-FRAC/REEP-FRAC" Hypothesis, Lunar and Planetary Science Conference.

Neal, C.R., 2001. Interior of the Moon: The presence of garnet in the primitive deep lunar mantle. Journal of Geophysical Research E: Planets 106, 27865-27885.

Neal, C.R., Donohue, P., Fagan, A.L., O'Sullivan, K., Oshrin, J., Roberts, S., 2015. Distinguishing between basalts produced by endogenic volcanism and impact processes: A non-destructive method using quantitative petrography of lunar basaltic samples. Geochimica et Cosmochimica Acta 148, 62-80.

Neal, C.R., Taylor, L.A., 1989b. Characterization of a pure urKREEP signature by identifying the" dregs" of the lunar magma ocean. Meteoritics 24, 308.

Neal, C.R., Taylor, L.A., 1992. Petrogenesis of mare basalts: A record of lunar volcanism. Geochimica et Cosmochimica Acta 56, 2177-2211.

Nemchin, A., Timms, N., Pidgeon, R., Geisler, T., Reddy, S., Meyer, C., 2009. Timing of crystallization of the lunar magma ocean constrained by the oldest zircon. Nature Geoscience 2, 133-136.

O'Neill, H.S.C., 1991. The origin of the moon and the early history of the earth-A chemical model. Part 1: The moon. Geochimica et Cosmochimica Acta 55, 1135-1157.

Papanastassiou, D., Wasserburg, G., 1975. Rb-Sr study of a lunar dunite and evidence for early lunar differentiates, Lunar and Planetary Science Conference Proceedings, pp. 1467-1489.

Powell, R., Holland, T., 1988. An internally consistent dataset with uncertainties and correlations: 3. Applications to geobarometry, worked examples and a computer program. Journal of metamorphic Geology 6, 173-204.

Prissel, T., Parman, S., Jackson, C., Rutherford, M., Hess, P., Head, J., Cheek, L., Dhingra, D., Pieters, C., 2014. Pink Moon: The petrogenesis of pink spinel anorthosites and implications concerning Mg-suite magmatism. Earth and Planetary Science Letters 403, 144-156.

Rapp, J., Draper, D., 2018. Fractional crystallization of the lunar magma ocean: Updating the dominant paradigm. Meteoritics & Planetary Science 53, 1432-1455.

Shearer, C.K., Elardo, S.M., Petro, N.E., Borg, L.E., McCubin, F.M., 2015. Origin of the lunar highlands Mg-suite: An integrated petrology, geochemistry, chronology, and remote sensing perspective. American Mineralogist 100, 294-325.

Shearer, C.K., Hess, P.C., Wieczorek, M.A., Pritchard, M.E., Parmentier, E.M., Borg, L.E., Longhi, J., Elkins-Tanton, L.T., Neal, C.R., Antonenko, I., Canup, R.M., Halliday, A.N., Grove, T.L., Hager, B.H., Lee, D.C., Wiechert, U., 2006. Thermal and magmatic evolution of the Moon, Reviews in Mineralogy and Geochemistry, pp. 365-518.

Shearer, C.K., Papike, J.J., 1999. Magmatic evolution of the Moon. American Mineralogist 84, 1469-1494.

Snape, J.F., Nemchin, A.A., Whitehouse, M.J., Merle, R.E., Hopkinson, T., Anand, M., 2019. The timing of basaltic volcanism at the Apollo landing sites. Geochimica et Cosmochimica Acta 266, 29-53.

Snyder, G.A., Taylor, L.A., Neal, C.R., 1992. A chemical model for generating the sources of mare basalts: Combined equilibrium and fractional crystallization of the lunar magmasphere. Geochimica et Cosmochimica Acta 56, 3809-3823.

Solomatov, V., 2000. Fluid dynamics of a terrestrial magma ocean. Origin of the Earth and Moon, 323-338.

Spera, F.J., 1992. Lunar magma transport phenomena. Geochimica et Cosmochimica Acta 56, 2253-2265.

Taylor, S.R., 1982. Lunar and terrestrial crusts: a constrast in origin and evolution. Physics of the Earth and Planetary Interiors 29, 233-241.

Thiemens, M.M., Sprung, P., Fonseca, R.O., Leitzke, F.P., Münker, C., 2019. Early Moon formation inferred from hafnium–tungsten systematics. Nature Geoscience 12, 696-700.

Toksőz, M., Press, F., Anderson, K., Dainty, A., Latham, G., Ewing, M., Dorman, J., Lammlein, D., Nakamura, Y., Sutton, G., 1972. Velocity structure and properties of the lunar crust. The moon 4, 490-504.

Tonks, W.B., Melosh, H.J., 1990. The physics of crystal settling and suspension in a turbulent magma ocean. Origin of the Earth, 151-174.

Walker, D., Longhi, J., Stolper, E.M., Grove, T.L., Hays, J.F., 1975. Origin of titaniferous lunar basalts. Geochimica et Cosmochimica Acta 39, 1219-1235.

Warren, P.H., 1985. The magma ocean concept and lunar evolution. Annual Review of Earth and Planetary Sciences 13, 201-240.

Warren, P.H., 1993. A concise compilation of petrologic information on possibly pristine nonmare Moon rocks. American Mineralogist 78, 360-376.

Warren, P.H., Wasson, J.T., 1979. The origin of KREEP. Reviews of Geophysics 17, 73-88.

Weber, R.C., Lin, P.-Y., Garnero, E.J., Williams, Q., Lognonne, P., 2011. Seismic detection of the lunar core. science 331, 309-312.

Whitney, D.L., Evans, B.W., 2010. Abbreviations for names of rock-forming minerals. American mineralogist 95, 185-187.

Wieczorek, M.A., Jolliff, B.L., Khan, A., Pritchard, M.E., Weiss, B.P., Williams, J.G., Hood, L.L., Righter, K., Neal, C.R., Shearer, C.K., 2006. The constitution and structure of the lunar interior. Reviews in mineralogy and geochemistry 60, 221-364.

Wieczorek, M.A., Neumann, G.A., Nimmo, F., Kiefer, W.S., Taylor, G.J., Melosh, H.J., Phillips, R.J., Solomon, S.C., Andrews-Hanna, J.C., Asmar, S.W., 2013. The crust of the Moon as seen by GRAIL. Science 339, 671-675.

Zuber, M.T., Smith, D.E., Lehman, D.H., Hoffman, T.L., Asmar, S.W., Watkins, M.M., 2013. Gravity Recovery and Interior Laboratory (GRAIL): Mapping the lunar interior from crust to core. Space Science Reviews 178, 3-24.

Figure captions

Fig. 1. Model set-up. We model equilibrium crystallisation of the first 50 vol.% of the silicate Moon to form a primitive peridotitic lower mantle, then fractional crystallisation of the upper 50 vol.% in separate 10 stages to form more evolved cumulated in the upper mantle, above which is the anorthosite flotation crust.

Fig. 2. Isochemical pressure–temperature phase diagrams (pseudosections) in the K_2O–Na_2O–CaO–FeO–MgO–Al_2O_3–SiO_2–TiO_2–Cr_2O_3 (KNCFMASTCr) system for the TWM (a) and LPUM (b) starting compositions, showing the calculated stability of equilibrium assemblages. In each case, the thick black line is the solidus, and the thick white line is the liquidus. The dashed white lines show calculated melt fractions (as mol.% ~ vol.%)—the thick white line shows 50 mol.% melt that corresponds to Stage 0 (see text for details). Mineral abbreviations follow Whitney and Evans (2010).

Fig. 3. Calculated abundance, density (ρ) and composition (*X*) of cumulate minerals formed by equilibrium crystallisation (Stage 0) of the first 50 vol.% of a LMO with the TWM (top) and LPUM (bottom) starting compositions as a function of pressure. Mineral abbreviations follow Whitney and Evans (2010).

Fig. 4. Calculated abundance of minerals formed by fractional crystallisation (stages 1–10) of the TWM (left) and LPUM (right) starting compositions as a function of the pressure. For each stage (representing 5 vol.% of the original LMO), the maximum and minimum pressures (P_{max} and P_{min}) correspond to the base and top of that stage after settling (for all minerals except quartz and plagioclase) and flotation (for plagioclase and quartz) of minerals formed during the preceding stage. See text for details. Also shown for comparison are the cumulate stratigraphies proposed by others. Mineral abbreviations follow Whitney and Evans (2010). The compositions modelled by Snyder et al. (1992) and Elkins-Tanton et al. (2011) are similar to that proposed by (Buck and Toksoz, 1980). That modelled by Charlier et al. (2018) is LPUM using a combined equilibrium and fractional crystallisation approach followed here. Those of Rapp and Draper (2018) consider fractional crystallisation of the LPUM and TWM compositions.

Fig. 5. Post-LMO crystallisation structure of the upper mantle and anorthosite crust formed by fractional crystallisation (stages 1–10; a), along with the calculated composition (*X*; b) and density (ρ; χ) of the minerals and melt. See text for details. Phase abbreviations follow Whitney and Evans (2010).

Fig. 6. Major oxide bulk compositions of melts (red) and residues (blue) for the TWM (left) and LPUM (right) starting compositions. The two starting bulk compositions are shown as grey squares. Also shown are two compositions proposed to represent pristine urKREEP by (Neal and Taylor, 1989a).

Fig. 7. Mean densities (ρ) of the midpoint of layers formed during stages 0–10 for the two modelled starting compositions (see also Fig. 5). The density profile of the pre-overturn cumulate of Elkins-Tanton et al. (2011) with between 1% (higher ρ) and 5% (higher ρ) interstitial liquid is also shown for reference (in grey).

Fig. 8. Composite *P–T* diagram showing the calculated phase assemblage for upper mantle cumulates produced during stages 1 to 10 in the two modelled stating compositions. The lowest *T* subsolidus assemblages are given in full. On heating, subsequent fields are labelled with the mineral that disappears (in the case of moving from a paler to a darker field) or appears (in the case of moving from a darker to a paler field). The *P–T* conditions of the solidus (thick black line) and liquidus ($F = 1$) are shown, along with the temperatures at which melt fractions of 5, 10, 20 and 30 mol.% are formed ($F = 0.05$, 0.10, 0.20, 0.30; white dots). Phase abbreviations follow Whitney and Evans (2010).

Fig. 9. Major oxide compositions of melts derived from partial melting of stage 1–10 residues (cumulates) for the two starting compositions at $F = 0.05$, 0.10, 0.20 and 0.30. Also shown are smoothed kernel density estimates of the compositions of low-Ti (blue 'clouds'), intermediate-Ti (grass-green), high-Ti (red) and KREEP (orange) basalts (data from the ApolloBasalt DB(v2) database at https://people.mines.edu/kcone/apollobasaltdb_v2_2020/), along with picritic green glasses (lime green) from Delano (1986) (see text for details).

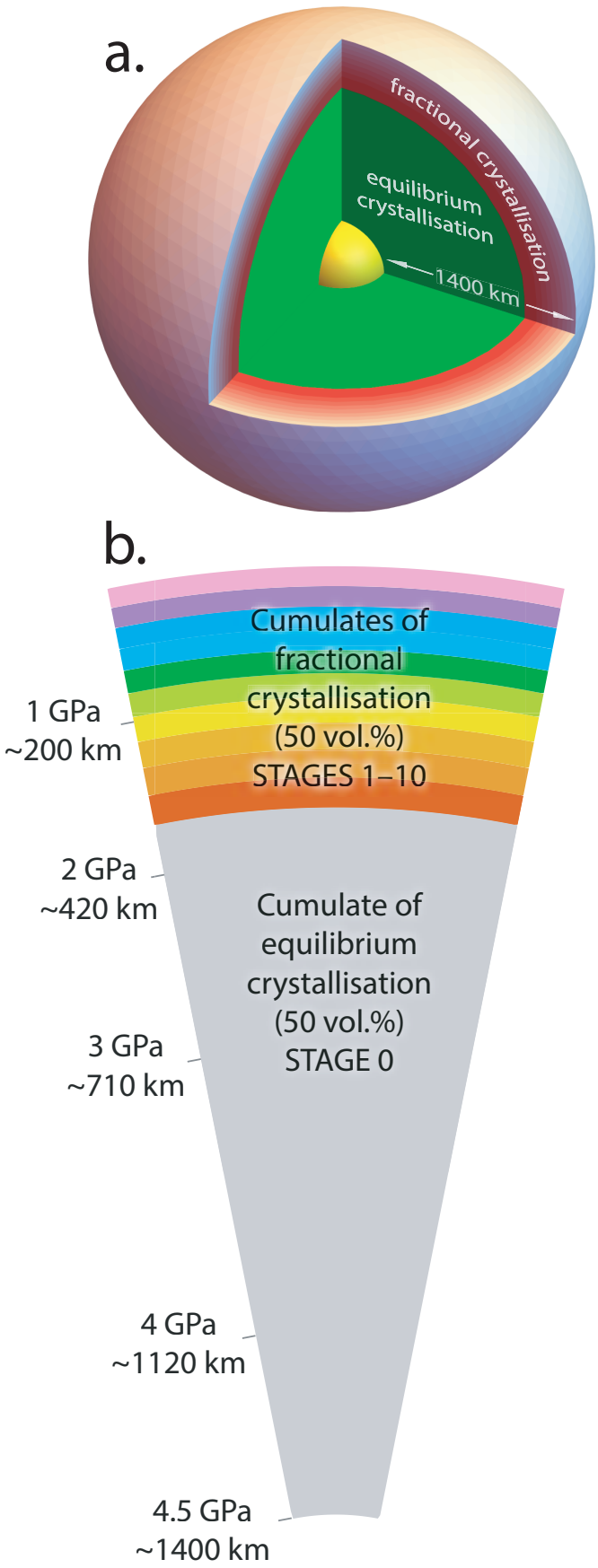

Johnson et al., Fig. 1

Figure 2

Click here to access/download;Figure;Fig. 2 (PT pseudos).eps

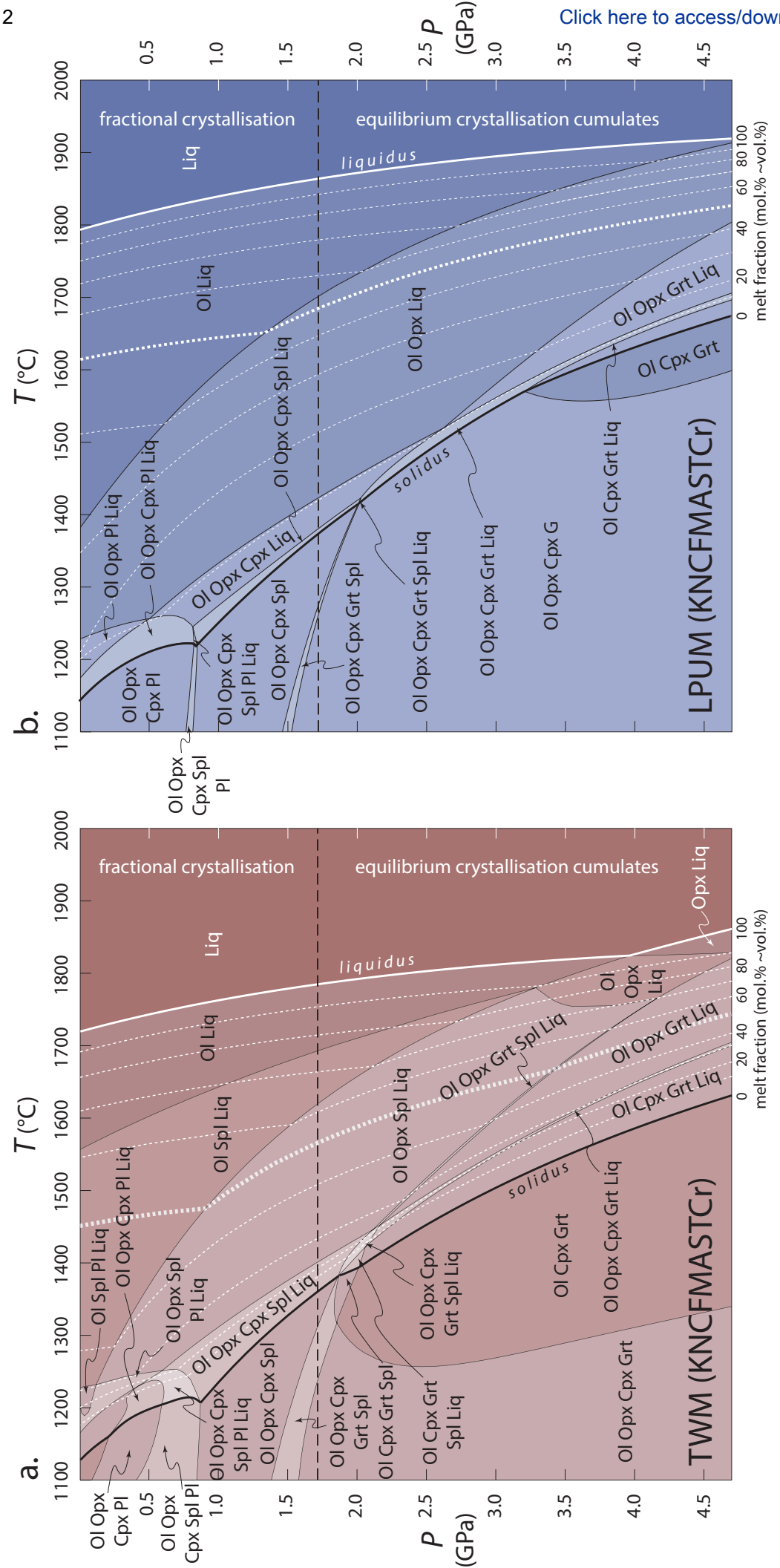

Johnson et al., Fig. 2

Figure 3

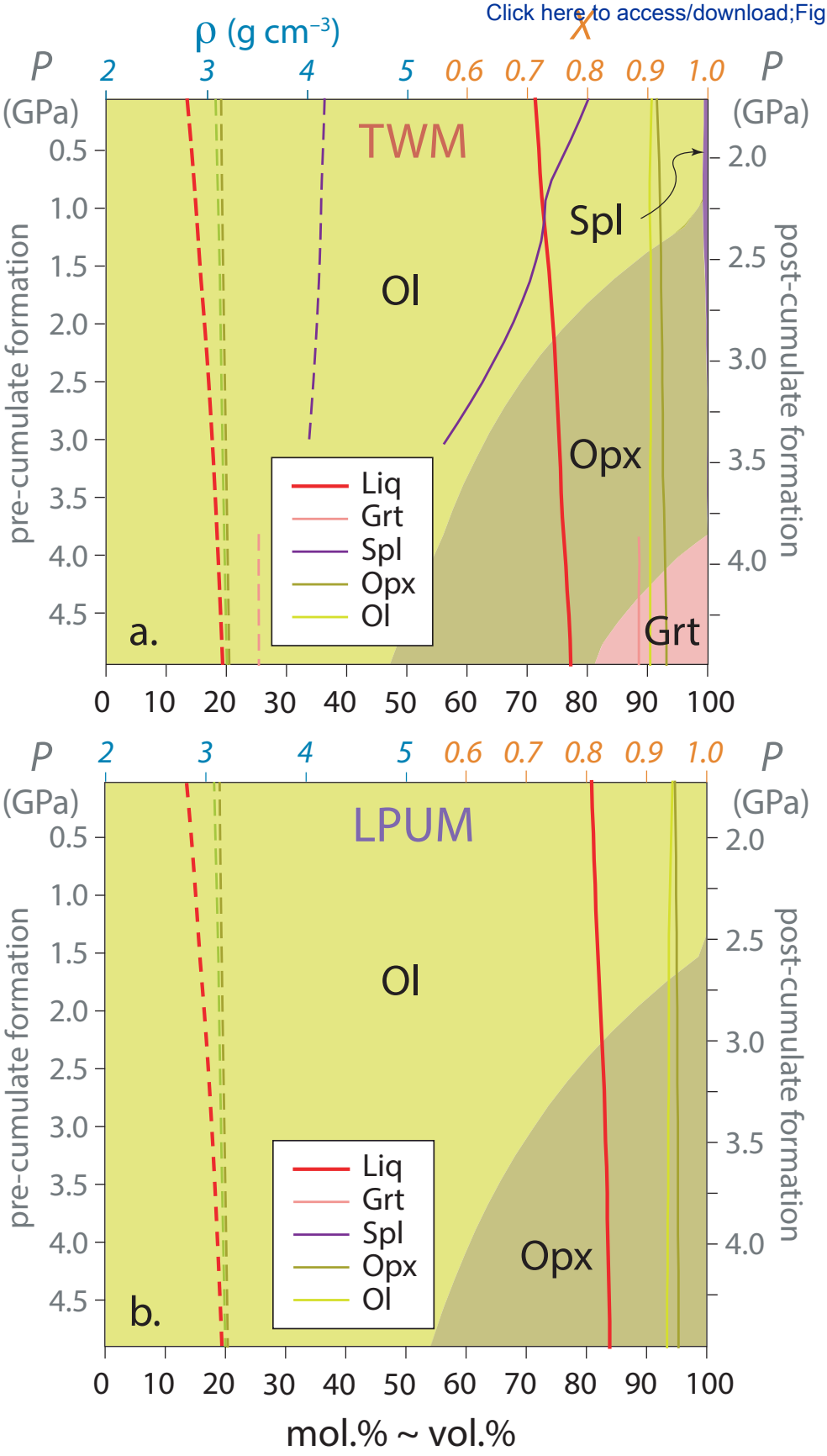

Johnson et al., Fig. 3

Figure 5

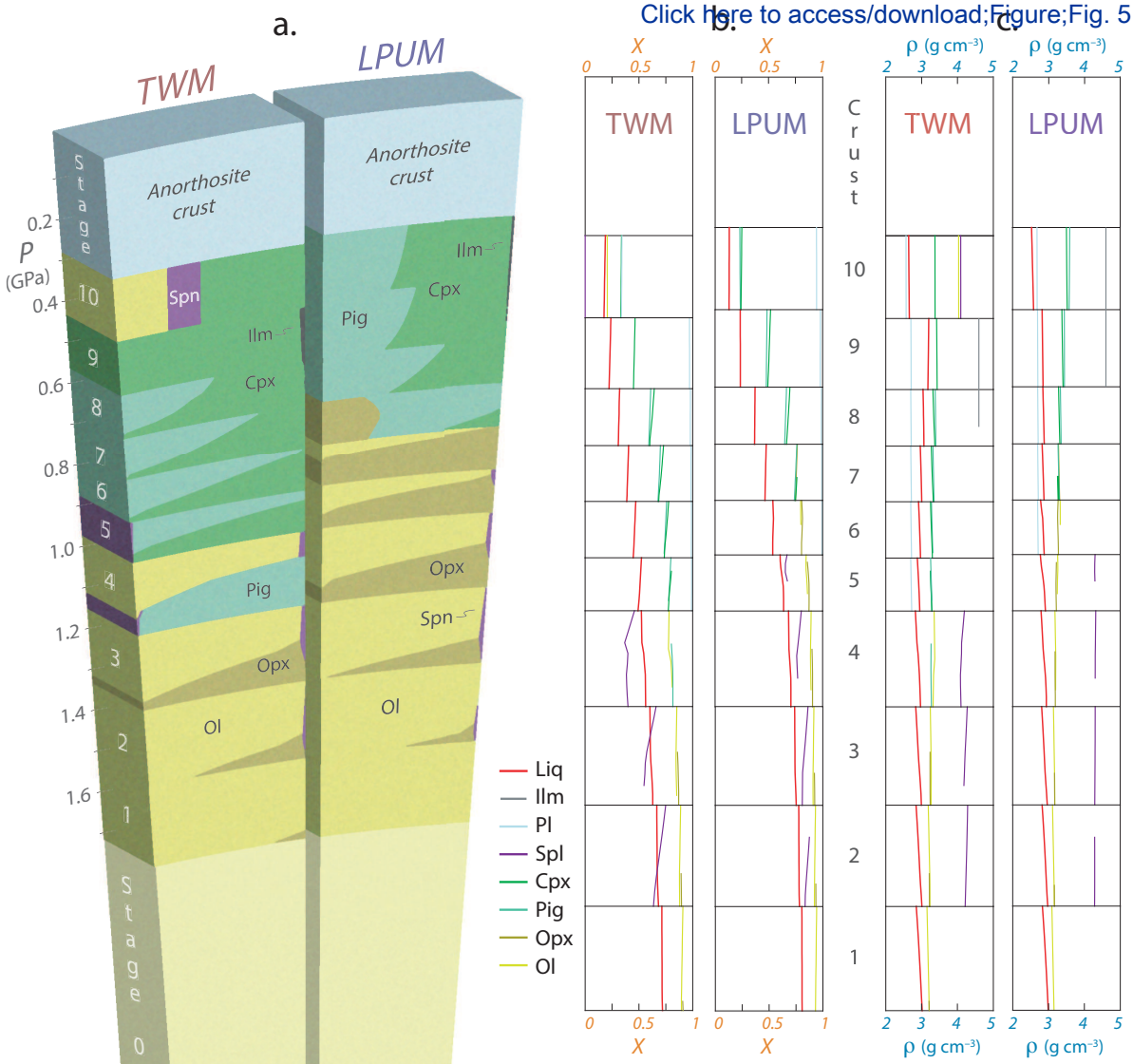

Figure 6

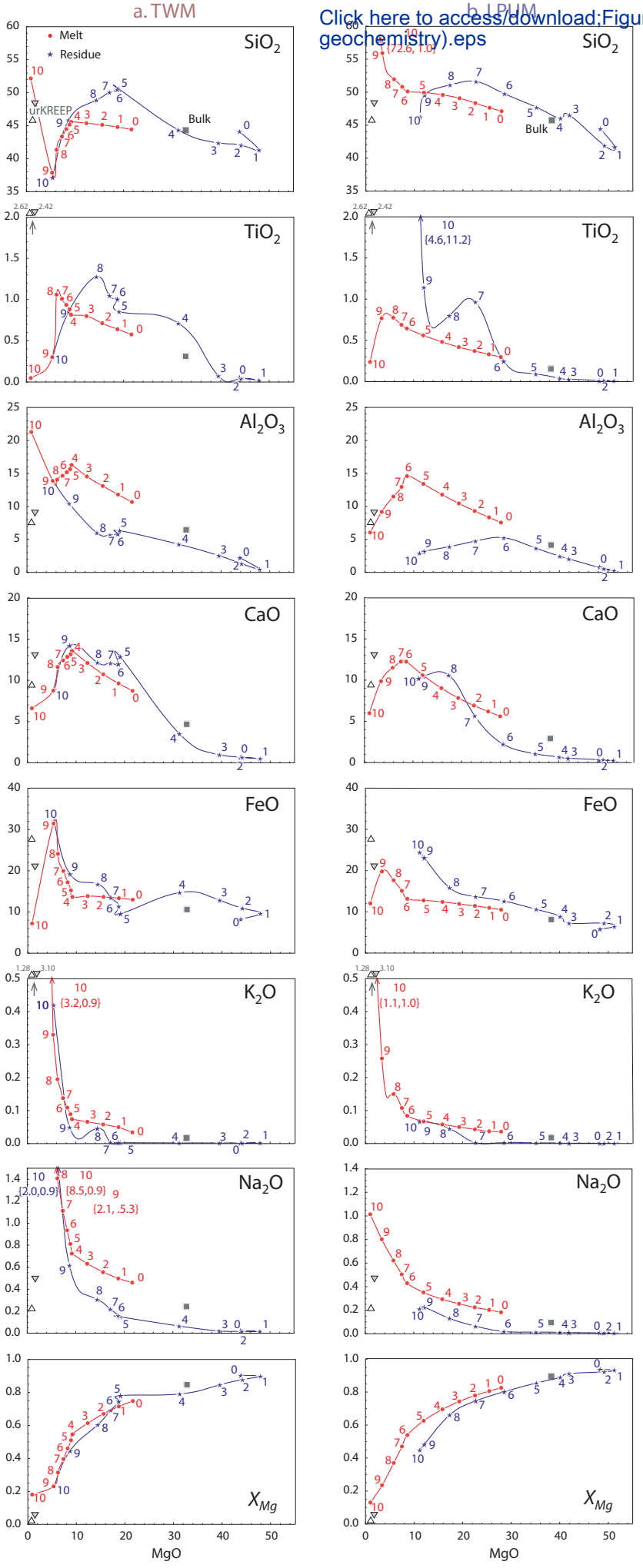

Johnson et al., Fig. 6

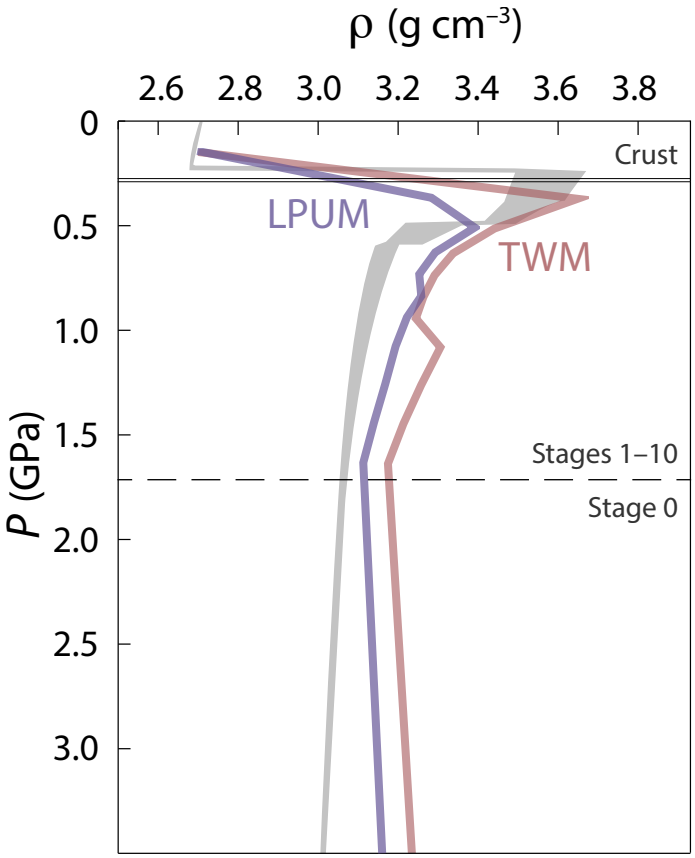

Johnson et al., Fig. 7

Figure 8

Click here to access/download;Figure;Fig. 8 (laura).eps

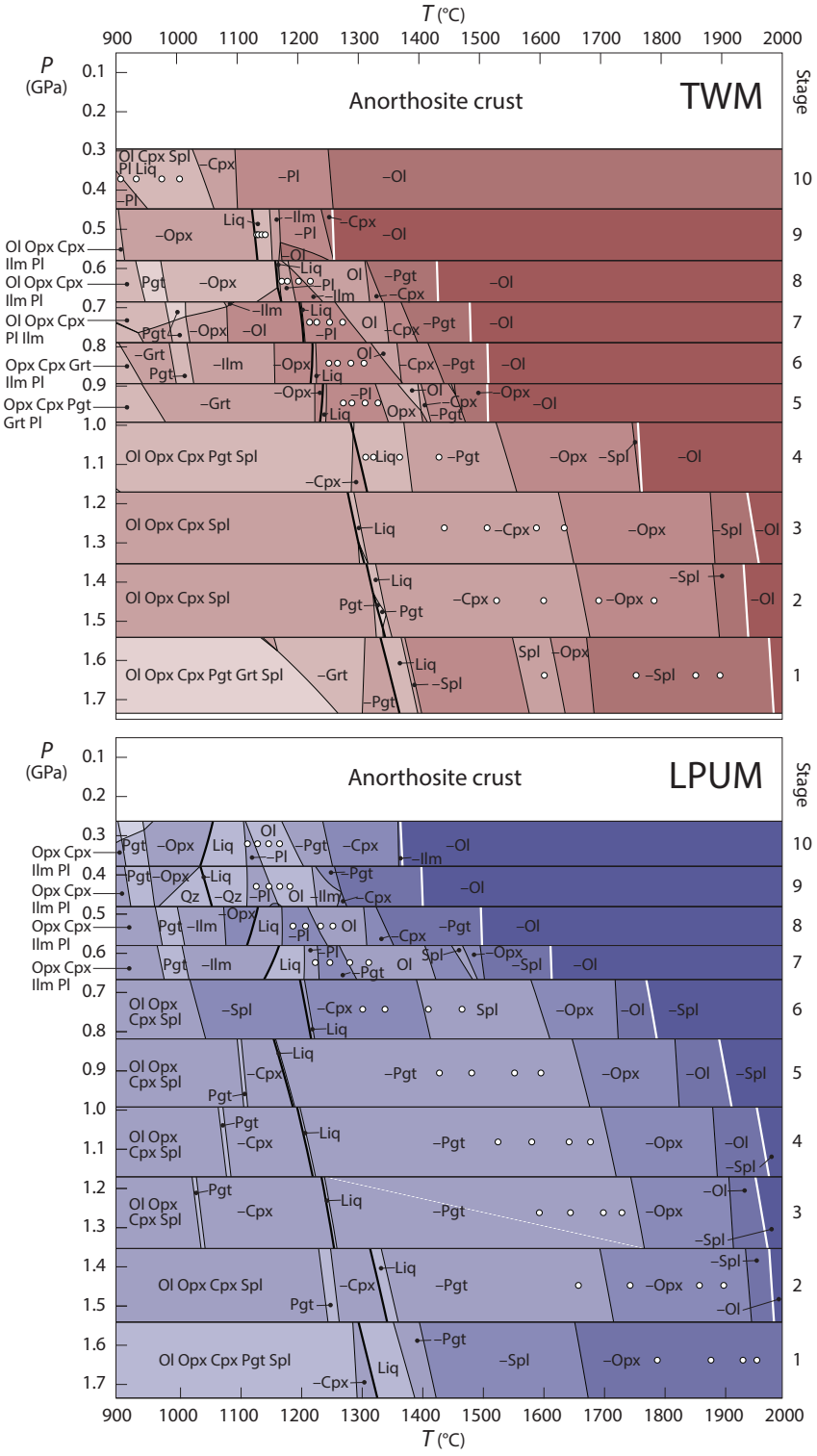

Johnson et al., Fig. 8

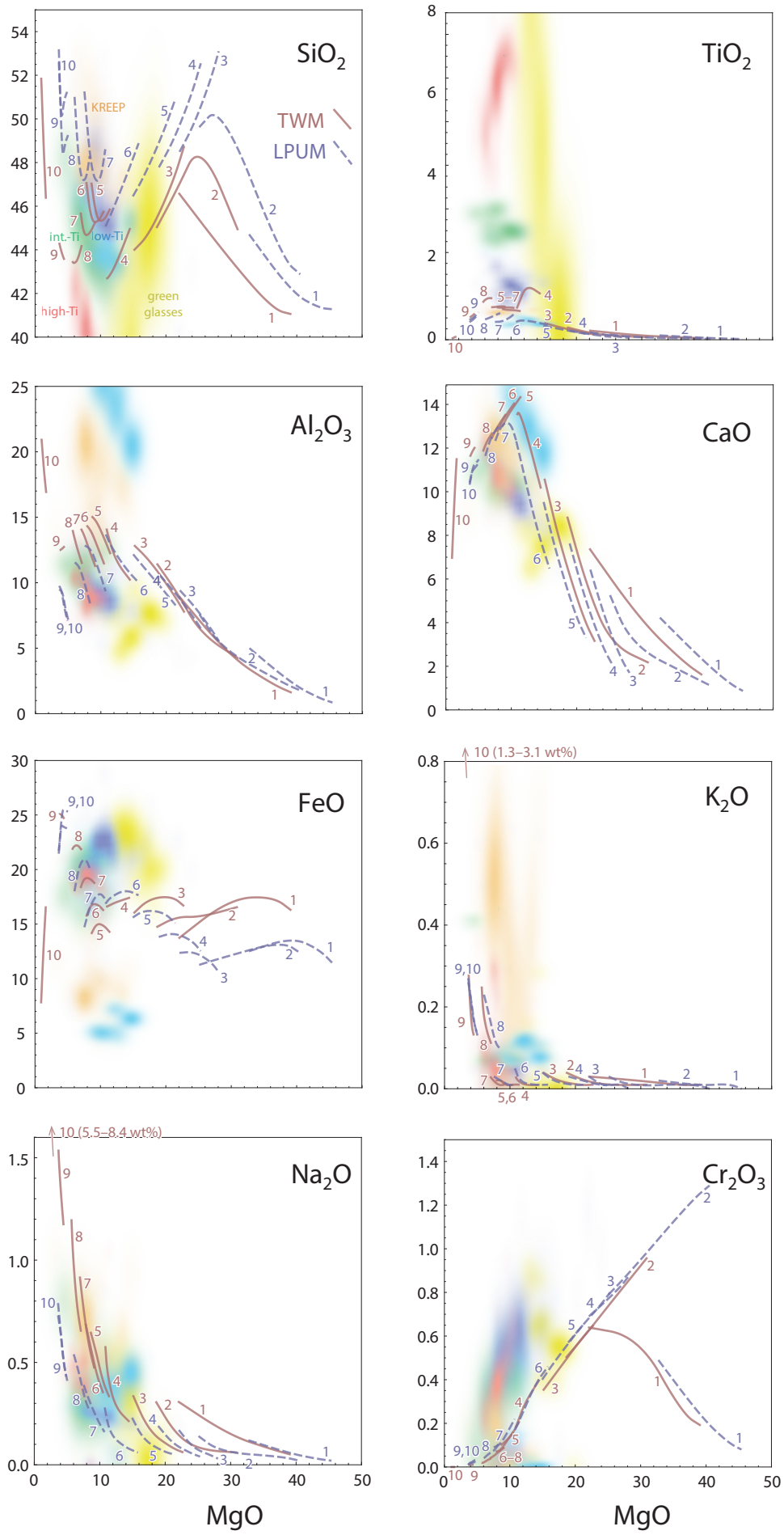

Johnson et al., Fig. 9